On the relation between Fourier and Walsh–Rademacher spectra for random fields

Anton Kutsenko[b,c,*], Sergey Danilov[a,b], Stephan Juricke[a,b], Marcel Oliver[b,c]

[a] *Alfred Wegener Institute for Polar and Marine Research, Bremerhaven, Germany*
[b] *Constructor University, Bremen, Germany*
[c] *Mathematical Institute for Machine Learning and Data Science, KU Eichstätt–Ingolstadt, Germany*

Abstract

We discuss relations between the expansion coefficients of a discrete random field when analyzed with respect to different hierarchical bases. Our main focus is on the comparison of two such systems: the Walsh–Rademacher basis and the trigonometric Fourier basis. In general, spectra computed with respect to one basis will look different in the other. In this paper, we prove that, in a statistical sense, the rate of spectral decay computed in one basis can be translated to the other. We further provide explicit expressions for this translation on quadrilateral meshes. The results are illustrated with numerical examples for deterministic and random fields.

Keywords: Random fields, spectra, Fourier basis, Walsh–Rademacher basis

1. Introduction

The statistical theory of turbulence makes heavy use of the spectral representation of random fields [e.g. 1, 2]. Modern computational methods, for reasons of parallelizability and modeling complex geometries, are predominantly based on local discrete operators on unstructured meshes. Thus, in order to consistently interpret computational results in the classical language of spectral analysis, suitable postprocessing is essential. One obvious route is to first interpolate from the unstructured mesh to a quadrilateral mesh, then perform classical Fourier analysis on the latter. The interpolation step, however, will have its own set of biases which, near the grid scale, is difficult to quantify. In this paper, we pursue a different approach, based on nothing more than a simple discrete averaging operation on a hierarchy of nested grids. The inferred spectra can then be translated consistently to the classical Fourier setting *in a statistical sense*. The translation function is computed explicitly in the simple case of nested square grids. More generally, it could be inferred computationally for complex grid geometries.

*Corresponding author
Email addresses: Anton.Kutsenko@ku.de (Anton Kutsenko), sergey.danilov@awi.de (Sergey Danilov), sjuricke@constructor.university (Stephan Juricke), marcel.oliver@ku.de (Marcel Oliver)

In more abstract language, we can sketch our main question as follows. Let u be some (random) field. Let $\{f_{\boldsymbol{k}}\}$ and $\{g_{\boldsymbol{k}}\}$ be some orthonormal bases, where $k = |\boldsymbol{k}|$ plays the role of an abstract wavenumber which imposes a total order on the bases. We expand the field in both cases, i.e., $u = \sum_{\boldsymbol{k}} u_{\boldsymbol{k}} f_{\boldsymbol{k}} = \sum_{\boldsymbol{k}} v_{\boldsymbol{k}} g_{\boldsymbol{k}}$. Now we try to compare $u_{\boldsymbol{k}}$ and $v_{\boldsymbol{k}}$ or, more precisely, the quantities $E_1(k) = \sum_{|\boldsymbol{k}|=k} u_{\boldsymbol{k}}^2$ and $E_2(k) = \sum_{|\boldsymbol{k}|=k} v_{\boldsymbol{k}}^2$ that represent the distribution of "energy" over length scales of order k^{-1}. One of the important questions is the following: if we observe $E_1(k) \propto k^{\alpha_1}$ and $E_2(k) \propto k^{\alpha_2}$, then what is the relation between α_1 and α_2? At which wavenumbers k and, generally, in which regimes can we state that $\alpha_1 \approx \alpha_2$, i.e., the spectral slopes computed in different basis systems are similar? Such a problem can hardly be resolved in full generality. Especially when the bases differ significantly, one can construct fields with a wide range of relations between α_1 and α_2. However, if we assume that the $u_{\boldsymbol{k}}$ are independently distributed random variables, relations between expected α_1 and α_2 can take a well-defined form.

In this paper, we focus on comparing two bases: the standard discrete Fourier trigonometric basis (F) on a square region of dimension d, and the Walsh–Rademacher (WR) basis generated by the indicator functions of the small sub-squares of that region. WR-basis functions take values $+1$ and -1 on each dyadic subpartition, and form an orthonormal basis for L^2 on the unit square. In the literature, this system is more commonly referred to as simply the Walsh system. Since Walsh functions are products of Rademacher functions and Rademacher was apparently well aware of this construction, see remarks in [3], we shall prefer the name "Walsh–Rademacher".

The WR-basis has several attractive features: First, it is a natural representation for cell-based quantities, particularly discrete finite-volume representations, without implying any specific degree of smoothness of an underlying continuum limit. Second, it is possible to establish a natural discrete total order on the WR-functions based on the size of the sub-domains on which they take a constant value. This implies that there exists a notion of spectrum based on the WR-scale decomposition in the sense defined above. Third, the orthogonal projector of a function onto a WR-subspace is simply the averaging operator onto the sub-domains at that level of the scale hierarchy. Thus, the spectrum of a function in the WR-representation can be computed by applying a sequence of averaging operators ordered by scale; we speak of the "resize-and-average" method. Finally, this construction does not require that the hierarchy of nested subdomains is regular. Only in this paper, we restrict to regular dyadic sub-partitioning of the square for the purpose of obtaining explicit formulae; computationally, no such restriction is required.

In the following, we consider random fields with a prescribed spectral slope in each of the two bases, diagnosed via the resize-and-average method. We focus on the case when the prescribed spectral slope is the same for all wavenumbers. This assumption will allow us to obtain an explicit closed-form dependency between the spectral slopes in the two bases.

As expected, when the prescribed spectral slope is prepared in the WR-basis, the resize-and-average method returns precisely this value in the statistical sense. However, for random fields that have a spectral slope $\alpha = \alpha_{\text{F}} > -3$ in the Fourier basis, the spectral slope

diagnosed via resize-and-average tends to

$$\alpha_{\mathrm{WR}} = -1 + \log_2 \frac{\displaystyle\int_{[0,\pi/2]^d} |\boldsymbol{x}|^{1-d+\alpha} \left(1 - \prod_{j=1}^{d} \cos^2 x_j\right) \mathrm{d}\boldsymbol{x}}{\displaystyle\int_{[0,\pi/2]^d} |\boldsymbol{x}|^{1-d+\alpha} \left(1 - \prod_{j=1}^{d} \cos^2(2x_j)\right) \prod_{j=1}^{d} \cos^2 x_j \, \mathrm{d}\boldsymbol{x}}, \tag{1}$$

in the limit of infinite resolution of the mesh, see Remark 4.3. When $\alpha_{\mathrm{F}} \leq -3$, $\alpha_{\mathrm{WR}} = -3$. Thus, in the limit of infinite resolution, the Walsh–Rademacher basis cannot be used to diagnose spectral slopes that are steeper than -3 in the Fourier basis; see, e.g., the discussion in [4]. The converse is also true: the Fourier basis cannot be used to diagnose WR spectral slopes steeper than a threshold, see Remark 4.7. In both cases, one of the reasons is that fields having zero spectral tails in one basis will have a non-zero spectral tail with some certain spectral exponent in another basis.

The key observation here is that for finite resolution, the behavior of α_{WR} near $\alpha = -3$ is smooth and we can also diagnose, albeit with increasingly poor conditioning, spectral slopes beyond the threshold via resize-and-average. While (1) may look complex, α_{WR} is readily computed and does not differ much from α_{F} for $\alpha \in (-3, 1)$. For example, in two dimensions the average discrepancy between α_{WR} and α_{F} does not exceed ten percent for $\alpha \in (-3, 1)$, see Fig. 1. The value $\alpha = -3$ is the unique spectral slope where (1) asserts the same spectral slope in the F and the WR-basis. Spectral slopes $\alpha \in (-3, -1)$ are of particular interests in the atmospheric and ocean sciences, specifically $\alpha = -5/3$ for fully developed turbulence in $d = 3$ [5, 6], $\alpha = -2$ or shallower for the horizontal wavenumber contribution to the Garrett–Munk spectrum for internal waves, see the review [7] citing [8, 9, 10], and $\alpha = -3$ for the enstrophy range in two-dimensional turbulence [11, 12, 13]. Perhaps the coincidence of slopes $\alpha = -3$ in F and WR basis is not an accident, but a consequence of statistical independence from each other of small-scale oscillations in a turbulent motion.

We note that for smooth functions on the continuum, the spectral energy density with respect to the WR-basis generically takes the form

$$E_{\mathrm{WR}}(k) \sim 2\, k^{-3} \, \langle \nabla u, \nabla u \rangle \tag{2}$$

as $k \to \infty$, where the non-negative quadratic form $\langle \cdot, \cdot \rangle$ which depends on the support of the WR-functions, see Section 3 below. In particular, for uniform square and triangular meshes, the quadratic form is given by

$$\langle \nabla u, \nabla u \rangle = \frac{1}{6} \int_{\Omega} \|\nabla u\|^2 \, \mathrm{d}\boldsymbol{x}. \tag{3}$$

Thus, the spectral slope α_{F} corresponding to a smooth field in the F-basis cannot be estimated in the WR-system as it would always yield $\alpha_{\mathrm{WR}} = -3$. One of the reasons is that the WR-functions are discontinuous and cannot approximate smooth fields on the continuum well. At the same time, our results show that on the contrary, as soon as the fields are discrete and defined only on mesh cells of finite size, we may obtain an estimate of α_{F} through

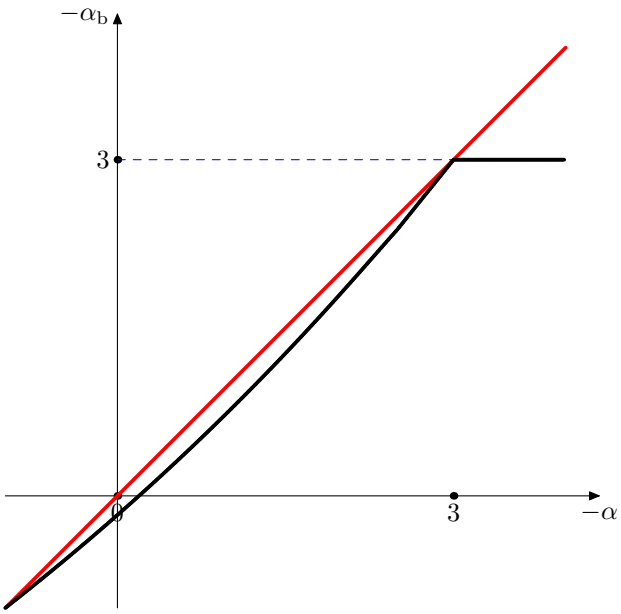

Figure 1: Spectral slopes α_b computed in different bases b=F (red line) and b=WR (black curve).

α_{WR}. However, when $\alpha \ll -3$, the connection between the F and the WR-scaling exponent becomes increasingly poorly conditioned.

One may ask why we choose the discrete Fourier basis, interpreted as L^2-functions by extending the grid values to a piecewise-constant function on small cubes, *not* as trigonometric interpolants. The reasons are twofold. First, the computational models sparking our interest are based on finite volume or low-order finite elements. Thus, the interpretation should keep the sense that a cell value is attributed to the geometric shape of a cell. Second, the interpretation as a smooth trigonometric interpolant would imply that the resize-and-average diagnosed spectral slope is always -3, which means that all problem-specific information near the original grid scale would get lost.

While we treat only the simplest case, namely regular dyadiacally nested meshes where explicit formulas can be derived, the underlying concepts can be applied on irregular meshes on complex domains just as well; see, e.g., the computation of resize-and-average spectra for dissipation power in a simulation of flow in an ocean-like channel discretized with a horizontally triangular mesh [14]. Other bases, e.g. higher-order polynomial bases, are also possible, but outside of the scope of this paper.

Our results generalize results obtained in, e.g., [15] who consider analogs of a 1D wavelet transform in the time-domain to multiple spatial dimensions. Such spectral wavelet analysis based on so-called "spectral windows" is similar to the use of WR-functions supported on intervals that are related to these spectral windows. Aspects of wavelet-based stochastic analysis of Gaussian random fields constructed via spherical harmonics is available in [16, 17, 18] and in some recent preprints [19, 20].

The main part of the manuscript is structured as follows. In Section 2, we describe abstract scale decompositions of Hilbert spaces. Section 3 illustrates concrete examples of

scale decompositions in the continuous case. The results resemble well-known facts from approximation theory where smooth functions are approximated by step functions, and also intersect with general provisions of homogenization theory; see, e.g., [21]. Section 4 is the main section of this paper, devoted to the statistical analysis of random fields with prescribed spectral slopes in the Fourier vs. the Walsh–Rademacher basis. Here, we discuss the statistical correlation between the slopes computed in different bases and give explicit asymptotic formulas in the spirit of classical probability theory (e.g. [22]). All the results obtained in Sections 2 and 4 are illustrated with concrete computational examples in Section 5. The paper conludes with a brief discussion and outlook.

2. Scale decompositions

A *scale decomposition* of a Hilbert space $\mathscr{H}$ is defined as the direct integral

$$\mathscr{H} = \int_{[0,\infty)}^{\oplus} \mathscr{H}_k \,\mathrm{d}\mu \tag{4}$$

over subspaces $\mathscr{H}_k$ (or spaces that are isomorphic to subspaces of $\mathscr{H}$) which contain the features with spatial length scale k^{-1}, where k is a non-negative scalar which we think of as an abstract wave number, and μ is a Borel measure on $[0,\infty)$. For background on the direct integral, a natural extension of the direct sum, see, e.g. [23]. A function $u \in \mathscr{H}$ has the scale representation

$$\hat{u}(k) = \mathcal{P}_k u, \tag{5}$$

where $\mathcal{P}_k$ is the orthogonal projector onto $\mathscr{H}_k$. This construction implies the Parseval identity

$$\|u\|_{\mathscr{H}}^2 = \int_0^\infty \|\hat{u}(k)\|^2 \,\mathrm{d}\mu. \tag{6}$$

Let $\mathcal{P}_{[k_1,k_2)}$ denote the orthogonal projector onto

$$\mathscr{H}_{[k_1,k_2)} = \int_{[k_1,k_2)} \mathscr{H}_k \,\mathrm{d}\mu. \tag{7}$$

Note that when μ has discrete components, we include the contribution from the lower scale k_1 but exclude the contribution from the upper scale k_2. The topic of this paper is the comparison of characterizations for the *cumulative spectral energy*

$$E_{[0,\kappa)} = \|\mathcal{P}_{[0,\kappa)} u\|^2 = \int_{[0,\kappa)} \|\hat{u}(k)\|^2 \,\mathrm{d}\mu. \tag{8}$$

We will focus on Hilbert spaces $\mathscr{H} = L^2(\Omega, \rho(\boldsymbol{x})\,\mathrm{d}\boldsymbol{x})$ and their subspaces on a domain $\Omega \subset \mathbb{R}^d$ where $\rho(\boldsymbol{x})$ is a non-negative density. For measurable subsets $A \subset \Omega$, we write

$$\langle\, \cdot \,\rangle_A = \int_A \cdot\, \rho(\boldsymbol{x})\,\mathrm{d}\boldsymbol{x}. \tag{9}$$

Then, in particular, the standard inner product for functions $f, g \in L^2(\Omega, \rho(\boldsymbol{x})\,\mathrm{d}\boldsymbol{x})$ – and on any of its subspaces – can be written $\langle f\,\overline{g}\rangle_\Omega$. The notion of orthogonality appearing throughout the paper is defined with respect to this inner product.

Next, we introduce our main examples of interest. In these examples, $\rho = \text{const}$, but sometimes taken different from $\rho = 1$ to better adapt to a particular setting. We start by writing the Fourier scale decomposition in the framework outlined above, then turn to the Walsh decomposition.

2.1. Fourier scale decomposition on $\Omega = \mathbb{R}^d$

We take $\rho = 1$, $\mathscr{H} = L^2(\mathbb{R}^d)$, and consider

$$\mathscr{H}_{2k} = \overline{\operatorname{span}}\{\mathrm{e}^{2\pi\mathrm{i}\,\boldsymbol{k}\cdot\boldsymbol{x}} \colon |\boldsymbol{k}| = k\}, \tag{10}$$

so that

$$\|\mathcal{P}_{2k}u\|^2 = \int_{\mathbb{S}_k} |\hat{u}(\boldsymbol{k})|^2\,\mathrm{d}S(\boldsymbol{k}), \tag{11}$$

$\mathrm{d}S(\boldsymbol{k})$ is the surface Lebesgue measure on the sphere of radius k and $\hat{u}(\boldsymbol{k})$ denotes the usual Fourier transform

$$\hat{u}(\boldsymbol{k}) = \langle u(\boldsymbol{x})\,\mathrm{e}^{-2\pi\mathrm{i}\,\boldsymbol{x}\cdot\boldsymbol{k}}\rangle_{\mathbb{R}^d}\,. \tag{12}$$

The implied measure in the abstract scale decomposition (6) is $\mu = \frac{1}{2}\,\mathrm{d}k$, i.e., half the Lebesgue measure on $[0, \infty)$. The factor 2 in the index on the left of (10) is a convenience factor. It is motivated by the observation that the harmonics $\sin(2\pi nx)$ and $\cos(2\pi nx)$ must be sampled at least once between adjacent zeros, so twice in each period. This definition fits best with the scaling functions on discrete meshes considered below.

2.2. Fourier scale decomposition on $\Omega = [0, 1]^d$

We take $\rho = 1$ and define the counting function

$$a(k) = \#A(k), \qquad A(k) = \{\boldsymbol{n} \in \mathbb{Z}^d \colon \|\boldsymbol{n}\|^2 = k^2\}, \tag{13}$$

where the symbol # denotes the number of elements of a set. Then the measure μ is a Delta measure located at the points where $a(k) \neq 0$ such that $\mu(\{2k\}) = a(k)$. The corresponding subspaces

$$\mathscr{H}_{2k} = \overline{\operatorname{span}}\{\mathrm{e}^{2\pi\mathrm{i}\,\boldsymbol{n}\cdot\boldsymbol{x}} \colon \boldsymbol{n} \in A(k)\} \tag{14}$$

are isomorphic to $\mathbb{C}^{a(k)}$. Using this identification, we can write

$$\mathcal{P}_{2k}u = (\hat{u}_{\boldsymbol{n}})_{\boldsymbol{n}\in A(k)}, \tag{15}$$

where

$$\hat{u}_{\boldsymbol{n}} = \langle u(\boldsymbol{x})\,\mathrm{e}^{-2\pi\mathrm{i}\,\boldsymbol{n}\cdot\boldsymbol{x}}\rangle_{[0,1]^d} \tag{16}$$

are the Fourier coefficients. Again, we use the factor 2 to better match the scaling functions to those on discrete meshes where samples corresponds to indicator functions on mesh cells. Using this convention, the scaling functions $\sin(2\pi nx)$ and $\cos(2\pi nx)$ correspond to sampling $2n$ times in each coordinate direction.

2.3. A variant of the Fourier scale decompositon for a diamond

Let us consider the domain consisting of two equilateral triangles

$$\Omega = \boldsymbol{S}[0,1]^2, \qquad \boldsymbol{S} = \begin{pmatrix} 1 & \frac{1}{2} \\ 0 & \frac{\sqrt{3}}{2} \end{pmatrix}. \tag{17}$$

The area of Ω is $\frac{\sqrt{3}}{2}$. Let $\mathscr{H}$ denote the Hilbert subspace of $L^2(\Omega, \frac{2}{\sqrt{3}}\,\mathrm{d}x\,\mathrm{d}y)$ spanned by the orthogonal family of cosine functions

$$c_{nm}(x,y) = \sqrt{2}\,\cos\Big(2\pi n x + \frac{4\pi m y}{\sqrt{3}}\Big), \qquad n,m \in \mathbb{N}. \tag{18}$$

Each c_{nm} has $2n$ and $2m$ roots within the fundamental domain along each axis. A function $u \in \mathscr{H}$ has representation

$$u(x,y) = \sum_{n,m\in\mathbb{N}} \hat{u}_{nm}\, c_{nm}(x,y), \qquad \hat{u}_{nm} \in \mathbb{C}, \tag{19}$$

so that the cumulative spectral energy is given by

$$E_{[0,2k)} = \sum_{n^2+m^2<k^2} |\hat{u}_{nm}|^2. \tag{20}$$

2.4. Walsh–Rademacher scale decompositions on arbitrary meshes

Along with continuous basis functions, step function bases are widespread in harmonic analysis. One of the classical examples is the Walsh–Rademacher basis consisting of piecewise constant functions on $[0,1]$ with dyadic points of discontinuity [24, 25]. We extend this idea to a multidimensional domain and arbitrary divisions of it, keeping the name Walsh–Rademacher basis. We consider discrete meshes where

$$\Omega = \bigcup_{c\in C} A_c \tag{21}$$

is a partition of the domain Ω onto a family of measurable disjoint sets, with C denoting the corresponding index set. Let us consider

$$\mathscr{L} = \overline{\operatorname{span}}\{\chi_{A_c} \colon c \in C\} \subset L^2(\Omega), \tag{22}$$

the Hilbert subspace of $L^2(\Omega)$ generated by the characteristic functions of the sets A_c. Given any scale decomposition of the form (4), which may or may not be defined with reference to a mesh, we say that the mesh $\{A_c \colon c \in C\}$ *resolves* the scales $[0,k)$ if

$$\mathscr{L} = \int_{[0,k)}^{\oplus} \mathscr{H}_k \,\mathrm{d}\mu. \tag{23}$$

Its orthogonal complement is

$$\mathscr{L}^\perp = \int_{[k,\infty)}^{\oplus} \mathscr{H}_k \,\mathrm{d}\mu \tag{24}$$

so that $\mathscr{L} \oplus \mathscr{L}^\perp = L^2(\Omega)$. Moreover,

$$\mathcal{P}_{[0,k)} u = \mathcal{P}_{\mathscr{L}} u = \sum_{c\in C} \frac{\langle u\,\chi_{A_c}\rangle_{A_c}}{\langle 1\rangle_{A_c}}\,\chi_{A_c}, \qquad \mathcal{P}_{[k,\infty)} u = u - \sum_{c\in C} \frac{\langle u\,\chi_{A_c}\rangle_{A_c}}{\langle 1\rangle_{A_c}}\,\chi_{A_c}, \tag{25}$$

and the corresponding norms (energies) are

$$\int_0^k \|\hat{u}(k)\|^2 \,\mathrm{d}\mu = \sum_{c\in C} \frac{\langle u\,\chi_{A_c}\rangle_{A_c}^2}{\langle 1\rangle_{A_c}}, \qquad \int_k^\infty \|\hat{u}(k)\|^2 \,\mathrm{d}\mu = \langle u^2\rangle_\Omega - \sum_{c\in C} \frac{\langle u\,\chi_{A_c}\rangle_{A_c}^2}{\langle 1\rangle_{A_c}}. \tag{26}$$

Now suppose that $\{A'_c \colon c \in C'\}$ is a submesh of $\{A_c \colon c \in C\}$ (i.e., every A_c is a union of some A'_c) and is such that it resolves the scales $[0, k')$ with $k' > k$ relative to the same scale decomposition. Then, by (26),

$$\int_k^{k'} \|\hat{u}(k)\|^2 \,\mathrm{d}\mu = \sum_{c\in C'} \frac{\langle u\,\chi_{A'_c}\rangle_{A'_c}^2}{\langle 1\rangle_{A'_c}} - \sum_{c\in C} \frac{\langle u\,\chi_{A_c}\rangle_{A_c}^2}{\langle 1\rangle_{A_c}}. \tag{27}$$

We can extend this idea developed for two meshes to the sequence of meshes $\{A_c\}$, $\{A'_c\}$, $\{A''_c\}$, …, each mesh containing the previous mesh as a submesh. Such sequence of meshes admits the construction of a common measure in the direct integral that ranks all these meshes on a common scale. However, it is generally not possible to define a single scale for all of the submeshes of a given mesh because two submeshes may not be submeshes of each other. A sufficient condition for the existence of a common scale is a total order of meshes with respect to the submesh relation.

3. Asymptotics in continuous case

For C^2-smooth functions u on a domain $\Omega \subset \mathbb{R}^d$, the remainder with respect to the Walsh–Rademacher scale decomposition typically has the form

$$\int_k^\infty \hat{u}^2 \,\mathrm{d}\mu = \frac{\langle \nabla u, \nabla u\rangle}{k^2} + o(k^{-2}), \tag{28}$$

where the positive definite form $\langle \nabla u, \nabla u\rangle$ depends on the geometry of the mesh. Let us consider some examples.

3.1. Square mesh

For a square mesh,

$$\langle \nabla u, \nabla u\rangle = \frac{1}{12}\int_\Omega \|\nabla u(\boldsymbol{x})\|^2 \,\mathrm{d}\boldsymbol{x}. \tag{29}$$

This formula is derived as follows. Using (26), we have

$$\int_k^\infty \hat{u}^2 \,\mathrm{d}\mu = \int_\Omega u^2 \,\mathrm{d}\boldsymbol{x} - k^d \sum_i \biggl(\int_{\Omega_i} u \,\mathrm{d}\boldsymbol{x}\biggr)^2 = \sum_i \biggl(\int_{\Omega_i} u^2 \,\mathrm{d}\boldsymbol{x} - k^d \biggl(\int_{\Omega_i} u \,\mathrm{d}\boldsymbol{x}\biggr)^2\biggr), \tag{30}$$

where Ω_i are disjoint cubes with edge length $1/k$ such that $\Omega = \cup_i \Omega_i$. Consider some Ω_i with minimal corner point $\boldsymbol{x}_i$. Using the Taylor expansion

$$u(\boldsymbol{x}_i + \boldsymbol{y}) = u(\boldsymbol{x}_i) + \nabla u(\boldsymbol{x}_i) \cdot \boldsymbol{y} + \boldsymbol{y}^\top \operatorname{Hess} u(\boldsymbol{x}_i) \boldsymbol{y} + o(\|\boldsymbol{y}\|^2), \tag{31}$$

we obtain

$$\begin{aligned}
&\int_{\Omega_i} u^2 \,\mathrm{d}\boldsymbol{x} - k^d \biggl(\int_{\Omega_i} u \,\mathrm{d}\boldsymbol{x}\biggr)^2 \\
&\qquad = \int_{[0,k^{-1}]^d} (\nabla u(\boldsymbol{x}_i) \cdot \boldsymbol{y})^2 \,\mathrm{d}\boldsymbol{y} - k^d \biggl(\int_{[0,k^{-1}]^d} \nabla u(\boldsymbol{x}_i) \cdot \boldsymbol{y} \,\mathrm{d}\boldsymbol{y}\biggr)^2 + o(k^{-d-2}) \\
&\qquad = \frac{k^{-d-2}}{12} \|\nabla u(\boldsymbol{x}_i)\|^2 + o(k^{-d-2}).
\end{aligned} \tag{32}$$

Note that the Hessian term contributes to both integrals in the first line of (32) at $O(k^{-d-2})$. These contributions, however, cancel exactly. Thus, substituting (32) into (30), we obtain the Riemann sum that gives (29). Below, we skip the derivation of similar formulas and formulate the final results only.

3.2. Rhomboid mesh

For a rhomboid mesh,

$$\langle \nabla u, \nabla u \rangle = \frac{1}{12} \int_\Omega \|\boldsymbol{S}^\top \nabla u(\boldsymbol{x})\|^2 \,\mathrm{d}\boldsymbol{x}, \tag{33}$$

where $\boldsymbol{S}[0,1]^d$ is the corresponding unit-rhombus. Formula (33) follows from (29) via a change of variables. In the special case of a diamond rhombus where $\boldsymbol{S}$ is given by (17),

$$\langle \nabla u, \nabla u \rangle = \frac{1}{48} \int_\Omega \bigl(5\,|\partial_x u|^2 + 2\sqrt{3}\,\partial_x u\,\partial_y u + 3\,|\partial_y u|^2\bigr) \,\mathrm{d}x\,\mathrm{d}y. \tag{34}$$

3.3. 2D square mesh divided into two triangles

Using the same arguments as in (32), but with every square divided into two triangles, we obtain

$$\langle \nabla u, \nabla u \rangle = \frac{1}{9} \int_\Omega (|\partial_x u|^2 - \partial_x u\,\partial_y u + |\partial_y u|^2) \,\mathrm{d}x\,\mathrm{d}y. \tag{35}$$

Note that a straightforward adaptation of (32) yields the prefactor $\frac{1}{18}$. To obtain the correct coefficient $\frac{1}{9}$, we note that if the square mesh resolves length scales $1/k$, then the division of one square into two equal triangles resolves length scales $1/(\sqrt{2}k)$, so that, to compensate, we need to replace $1/k$ by $\sqrt{2}/k$ on the right hand side of formula (28).

3.4. 2D equilateral triangular mesh

By analogy with (33), substituting $\boldsymbol{S}^\top \nabla u$, where $\boldsymbol{S}$ is given by (17), for ∇u in (35), we obtain the quadratic form for the uniform triangular mesh,

$$\langle \nabla u, \nabla u \rangle = \frac{1}{12} \int_\Omega \|\nabla u(\boldsymbol{x})\|^2 \, \mathrm{d}\boldsymbol{x}. \tag{36}$$

4. Statistical analysis on finite meshes

We now turn to the setting of finite meshes, with cell values interpreted as constant on mesh cells. This point of view is consistent with the representation by Walsh–Rademacher basis functions, see Section 2.4. Of course, the choice of orthonormal basis is not unique and there are many other scale decompositions in the sense of Section 2. The respective spectra will generally not coincide, but we ask the question of how one may relate to the other. As we shall see, the difference tends to be small when the spectrum is shallow, but is significant in the case of rapid spectral decay.

In this section, we restrict the discussion to dyadically nested square meshes as they are simple to describe and it is possible to obtain explicit results. Computationally, however, the ideas extend to arbitrary meshes, as will be discussed in Section 6 at the end of this paper. On quadrilateral meshes, the second canonical choice of basis is the discrete Fourier basis. At the finest scale, we retain the interpretation of constant values on cells so that, independent of the choice of discrete basis, we speak about the same piecewise constant function in L^2.

The fundamental object in our discussion is the "resize-and-average" operator. To be definite, consider a d-dimensional square mesh consisting of $(2N)^d$ identical cubes. Let u be a field, constant on each of the cubes. Merging 2^d neighboring cubes into one, we obtain N^d large cubes instead of $(2N)^d$ small cubes. This is the resize step, see Fig. 2. Taking the average over the 2^d neighboring values of the field u, we obtain a new field $v \equiv \mathcal{A}_{2N} u$ which is piecewise constant on the N^d large cubes. The linear operator $\mathcal{A}_{2N}$ is the "resize-and-average" operator. It is easily seen that it coincides with a spectral projector in the Walsh–Rademacher basis. Its description in the Fourier basis is more complicated, but we shall show that, in a statistical sense as $N \to \infty$, its action can be related to the Fourier spectral decomposition.

4.1. Scaling exponent in general

We assume that the measure μ, see (4), is proportional to the Lebesgue measure. Let u be some field. Suppose that $\|\hat{u}(k)\|^2$, see (5), is proportional to k^α. Then the exponent α is given by

$$\alpha = -1 + \log_2 \frac{\|\mathcal{P}_{[2^n, 2^{n+1})} u\|^2}{\|\mathcal{P}_{[2^{n-1}, 2^n)} u\|^2}, \tag{37}$$

which follows immediately from (8) and the fact that

$$\|\mathcal{P}_{[a,b)} u\|^2 = \int_a^b \|\hat{u}(k)\|^2 \, \mathrm{d}\mu(k) \propto \int_a^b k^\alpha \, \mathrm{d}k = \frac{b^{\alpha+1} - a^{\alpha+1}}{\alpha + 1} \tag{38}$$

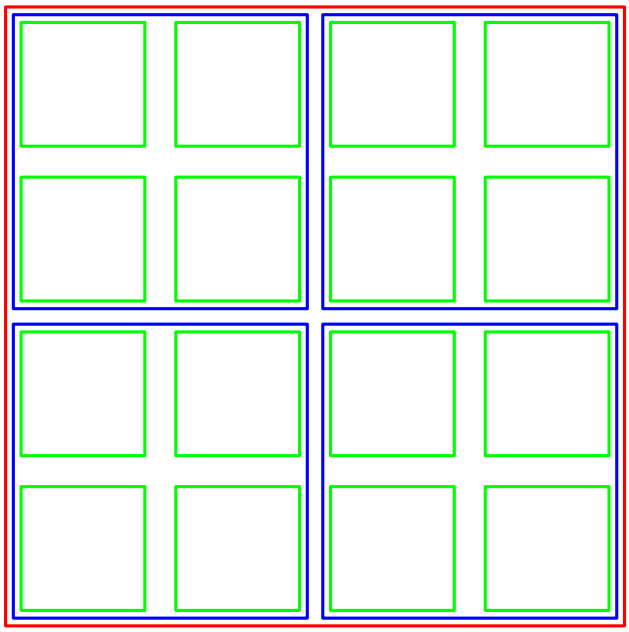

Figure 2: The initial field u is constant on each of the green squares. The resized and averaged field $\mathcal{A}_4 u$ is constant on each of the blue squares. The constants in the blue cubes are averages over the respective green squares. The next iteration $\mathcal{A}_2\mathcal{A}_4 u$ is constant on the red square. The constant in the red square is an average over the blue squares. There are no gaps between squares, the gaps are shown for ease of illustration.

for $a, b > 0$ and $\alpha \neq -1$. A similar computation shows that (37) remains valid when $\alpha = -1$.

Note that this is only one variant of a family of similar formulas. We provide this variant because it is adapted to the spectral decomposition in the Walsh–Rademacher orthogonal basis.

4.2. Scaling exponent in the Walsh–Rademacher basis

Consider the domain $[0, H]^d \subset \mathbb{R}^d$, $H > 0$, $d \in \mathbb{N}$, partitioned into a standard cubical mesh of size H/N with $N = 2^n$ for $n \in \mathbb{N}_0$. We define the family of Hilbert spaces

$$\mathscr{W}_{[1,N]} = \overline{\text{span}}\{\text{indicator functions of mesh cells of size } H/N\}, \tag{39}$$

and set $\mathscr{W}_k = \mathscr{W}_{[1,k]} \ominus \mathscr{W}_{[1,k/2]}$, so that $\mathscr{W}_{[1,N]}$ splits into orthogonal subspaces

$$\mathscr{W}_{[1,N]} = \mathscr{W}_{2^0} \oplus \cdots \oplus \mathscr{W}_{2^n}. \tag{40}$$

We write bas$\mathscr{W}_k$ to denote any fixed orthonormal basis of $\mathscr{W}_k$, the particular choice will not matter. Note that there is no way to assign wave numbers k in the open interval $(2^n, 2^{n+1})$, so that we may identify $\mathscr{W}_{2^n} \equiv \mathscr{W}_{[2^n, 2^{n+1})}$ and $\mathscr{W}_{[1,N]} \equiv \mathscr{W}_{[1,2N)}$ in the notation of Section 2.

For every $J = 2^j$, the resize-and-average operator $\mathcal{A}_J$ is defined as the orthogonal projector of $\mathscr{W}_{[1,J]}$ onto $\mathscr{W}_{[1,J/2]}$. Referring again to the notation of Section 2, we may write $\mathcal{A}_J = \mathcal{P}_{[1,2^j)}$. Equivalently, the operator $\mathcal{A}_J$ averages the values of 2^d neighboring small

cubes of size $H/2^j$ to larger cubes of size $H/2^{j-1}$, as illustrated in Fig. 2. This equivalent description provides an easy method for numerical computation and will also be used to write out the explicit formula for $\mathcal{A}_J$ in the Fourier basis, see (59) below. It is convenient to consider projectors $\mathscr{W}_{[1,N]} \to \mathscr{W}_{[1,2^{-i}N]}$ given by

$$\mathcal{A}^i = \mathcal{A}_{2^{1-i}N} \cdots \mathcal{A}_{2^{-1}N} \, \mathcal{A}_N \tag{41}$$

for $1 \le i \le n$ and $\mathcal{A}^0$ is understood as the the identity operator acting on $\mathscr{W}_{[1,N]}$. We can then define the spectral energy at scale 2^j,

$$E_j \equiv \|\mathcal{P}_{[2^j,2^{j+1})} u\|^2 = \|\mathcal{A}^{n-j} u\|^2 - \|\mathcal{A}^{n-j+1} u\|^2 \tag{42}$$

for $j = 1, \dots, n$, so that the discrete spectral energy *density* is given by

$$S_j = (2^{j+1} - 2^j)^{-1} \, E_j = 2^{-j} \, E_j. \tag{43}$$

Finally, we define the diagnosed Walsh–Rademacher scaling exponent at scale j as

$$\alpha_{\mathrm{c}}^{\mathrm{WR}}(j) = \left. \frac{\Delta \ln S(k)}{\Delta \ln k} \right|_{k=2^j} = \frac{\ln S_j - \ln S_{j-1}}{\ln 2^j - \ln 2^{j-1}} = \log_2 \frac{S_j}{S_{j-1}} = -1 + \log_2 \frac{E_j}{E_{j-1}}. \tag{44}$$

This scaling exponent is easily computationally accessible.

If u is a random field, then $\alpha_{\mathrm{c}}^{\mathrm{WR}}(j)$ is a random variable. If, under suitable assumptions, $\mathbb{E}E_j$ and $\mathbb{E}E_{j-1}$ exist as non-zero finite numbers, we can also define the "expected" Walsh–Rademacher scaling exponent as

$$\alpha_{\mathrm{e}}^{\mathrm{WR}}(j) = -1 + \log_2 \frac{\mathbb{E}E_j}{\mathbb{E}E_{j-1}}. \tag{45}$$

Then

$$\alpha_{\mathrm{c}}^{\mathrm{WR}}(j) - \alpha_{\mathrm{e}}^{\mathrm{WR}}(j) = \log_2\left(1 + \frac{E_j - \mathbb{E}E_j}{\mathbb{E}E_j}\right) - \log_2\left(1 + \frac{E_{j-1} - \mathbb{E}E_{j-1}}{\mathbb{E}E_{j-1}}\right). \tag{46}$$

In practical applications, N will be fixed. In our theoretical analysis, however, we consider an infinite sequence of mesh refinements and consider j a function of N in the limit $N \to \infty$. Then (46) shows that, in this limit, $\alpha_{\mathrm{c}}^{\mathrm{WR}}(j) - \alpha_{\mathrm{e}}^{\mathrm{WR}}(j) \to 0$ in probability if $\mathbb{E}E_i$ are bounded from below with $\operatorname{Var} E_i \to 0$ for $i = j-1, j$.

4.3. Statistical model in the Walsh–Rademacher basis

In the following, we first look at the statistics of the Walsh–Rademacher scaling exponent near the tail of the finite spectral distribution, where we write, for short, $\alpha_{\mathrm{c}}^{\mathrm{WR}} = \alpha_{\mathrm{c}}^{\mathrm{WR}}(n)$ and, likewise, $\alpha_{\mathrm{e}}^{\mathrm{WR}} = \alpha_{\mathrm{e}}^{\mathrm{WR}}(n)$. We first show that for random fields that have a well-defined scaling exponent α with respect to the Walsh–Rademacher basis, the diagnosed Walsh–Rademacher scaling exponent $\alpha_{\mathrm{c}}^{\mathrm{WR}}$ recovers α with high probability.

Concretely, we consider random fields

$$u = \bar{u} + \sum_{w \in \mathrm{bas}\mathscr{W}_{2^{n-1}}} 2^{\beta(n-1)}\, \zeta_w\, w + \sum_{w \in \mathrm{bas}\mathscr{W}_{2^n}} 2^{\beta n}\, \zeta_w\, w, \tag{47}$$

where $\bar{u} \in \mathscr{W}_{[1,2^{n-2}]}$ is some given large-scale component and the ζ_w are independent identically distributed random variables having zero mean and a finite second moment $D_2 > 0$. Thus, u has a spectral tail with decay exponent $\beta = (\alpha - d + 1)/2$, engineered such that the energy distribution $\|\hat{u}(k)\|^2$ is proportional to k^α in the deterministic case $\zeta_w = \mathrm{const}$. Moreover, it is easy to see that this construction ensures that the expected Walsh–Rademacher exponent coincides with the deterministic rate of spectral decay, i.e., $\alpha_{\mathrm{e}}^{\mathrm{WR}} = \alpha$.

For the diagnosed Walsh–Rademacher exponent, we have

$$\begin{aligned} \alpha_{\mathrm{c}}^{\mathrm{WR}} &= -1 + \log_2 \frac{\sum_{w \in \mathrm{bas}\mathscr{W}_{2^n}} 2^{2\beta n}\, \zeta_w^2}{\sum_{w \in \mathrm{bas}\mathscr{W}_{2^{n-1}}} 2^{2\beta(n-1)}\, \zeta_w^2} \\ &= \alpha + \log_2 \frac{(\dim \mathscr{W}_{2^n})^{-1} \sum_{w \in \mathrm{bas}\mathscr{W}_{2^n}} \zeta_w^2}{(\dim \mathscr{W}_{2^{n-1}})^{-1} \sum_{w \in \mathrm{bas}\mathscr{W}_{2^{n-1}}} \zeta_w^2}, \end{aligned} \tag{48}$$

since $\dim \mathscr{W}_{2^i} = 2^{di} - 2^{d(i-1)}$ for $i \geq 1$. Hence,

$$\begin{aligned} \alpha_{\mathrm{c}}^{\mathrm{WR}} - \alpha &= \log_2 \frac{D_2 + (\dim \mathscr{W}_{2^n})^{-1} \sum_{w \in \mathrm{bas}\mathscr{W}_{2^n}} (\zeta_w^2 - D_2)}{D_2 + (\dim \mathscr{W}_{2^{n-1}})^{-1} \sum_{w \in \mathrm{bas}\mathscr{W}_{2^{n-1}}} (\zeta_w^2 - D_2)} \\ &= \eta_n - \eta_{n-1} + O(\eta_n^2) + O(\eta_{n-1}^2), \end{aligned} \tag{49}$$

where the random variables η_n and η_{n-1} are independent and given by

$$\eta_i = \frac{\sum_{w \in \mathrm{bas}\mathscr{W}_{2^i}} (\zeta_w^2 - D_2)}{D_2 \,\ln 2\, \dim \mathscr{W}_{2^i}}. \tag{50}$$

Due to the weak law of large numbers, $\alpha_{\mathrm{c}}^{\mathrm{WR}} \to \alpha$ in probability as $n \to \infty$. If we further assume that the fourth moment $D_4 = \mathbb{E}\zeta_w^4$ is finite, the central limit theorem implies that

$$D_2 \,\ln 2 \sqrt{\dim \mathscr{W}_{2^i}}\, \eta_i \to \mathscr{N}(0, D_4 - D_2^2)\,, \tag{51}$$

so that, summing up the two independent limiting Gaussians in (49), we obtain

$$2^{\frac{nd}{2}} (\alpha_{\mathrm{c}}^{\mathrm{WR}} - \alpha) \to \mathscr{N}\left(0, \frac{(D_4 - D_2^2)\,(4^d + 2^d)}{(D_2 \ln 2)^2\,(2^d - 1)}\right) \tag{52}$$

in distribution as $n \to \infty$.

The observation that $\alpha_{\mathrm{c}}^{\mathrm{WR}} \to \alpha$ in the sense stated is no surprise because the statistical model and the diagnostics were set up with respect to the same scale decomposition. In the next section, we turn to the situation where the statistical model is set up in the Fourier scale decomposition, as in the classical theory of random fields (e.g. [26]), but we keep the diagnostics relative to the Walsh–Rademacher scale decomposition.

4.4. Statistical model in the Fourier basis

As usual, we write $\mathbb{Z}_N = \mathbb{Z}/N\mathbb{Z}$. We introduce the Hilbert space $\mathscr{L}_N \cong \mathbb{C}^{N^d}$ where the elements are indexed from the set $\mathbb{Z}_N^d/N$, equipped with inner product and norm

$$\langle u, v\rangle_N = \frac{1}{N^d} \sum_{\boldsymbol{x}\in\mathbb{Z}_N^d/N} u(\boldsymbol{x})\, v^*(\boldsymbol{x}), \qquad \|u\|_N^2 = \langle u, u\rangle_N \tag{53}$$

for $u, v \in \mathscr{L}_N$, with $*$ denoting complex conjugation. We consider the orthonormal discrete Fourier basis $\{f_{N,\boldsymbol{k}} \colon \boldsymbol{k} \in \mathbb{Z}_N^d\}$ with

$$f_{N,\boldsymbol{k}}(\boldsymbol{x}) = \exp(2\pi \mathrm{i} \boldsymbol{k}\cdot\boldsymbol{x}), \quad \boldsymbol{x} \in \mathbb{Z}_N^d/N. \tag{54}$$

Note that $\mathscr{L}_N$ is isomorphic to $\mathscr{W}_{[1,N]}$; the difference lies only in the choice of basis. To make the correspondence precise, we identify a vector $\boldsymbol{u} \in \mathscr{L}_N$ with the function u on $[0,1)^d$ that takes the constant value $u(\boldsymbol{x})$ on each half-open cube $\boldsymbol{x} + [0, \frac{1}{N})^d$, $\boldsymbol{x} \in \mathbb{Z}_N^d/N$.

In the following we assume, for simplicity, that N is even. We write

$$u = \sum_{\boldsymbol{k}\in\mathbb{Z}_N^d} u_{\boldsymbol{k}}\, f_{N,\boldsymbol{k}} \in \mathscr{L}_N \tag{55}$$

and assume that the Fourier coefficients $u_{\boldsymbol{k}}$ are random variables, setting $u_{\boldsymbol{k}} = \sigma_{\boldsymbol{k}}\, \zeta_{\boldsymbol{k}}$ where $\sigma_{\boldsymbol{k}} > 0$ and $\zeta_{\boldsymbol{k}}$ are identically independently distributed random variables with zero mean, variance 1, and finite moments up to order four. Then $u_{\boldsymbol{k}}$ has zero mean and variance $\sigma_{\boldsymbol{k}}^2$.

Our assumption on the $\sigma_{\boldsymbol{k}}$ is motivated by the alternative identification of $\mathscr{L}_N$ with trigonometric interpolants of Sobolev-class functions. Then the index range $\frac{N}{2}, \dots, N-1$ represents wave numbers $k = -\frac{N}{2}+1, \dots, -1$, so we assume the power law scaling

$$\sigma_{\boldsymbol{k}} = \begin{cases} \left(\frac{1}{N}\right)^{\frac{d}{2}} \left(\frac{|\boldsymbol{k}|}{N}\right)^{\frac{\alpha-d+1}{2}} & \text{for } \alpha > -3, \\ N\,|\boldsymbol{k}|^{\frac{\alpha-d+1}{2}} & \text{for } \alpha \le -3 \end{cases} \tag{56}$$

for $\boldsymbol{k} \in \mathbb{Z}_{N/2}^d \setminus \{\boldsymbol{0}\}$, and $\sigma_{\boldsymbol{k}} = 0$ otherwise. Here, to simplify the exposition, we have restricted the set of active wavenumbers to the first hyperoctant. Of course, all results and conclusions remain unchanged when mirroring this pattern of spectral decay into the other hyperoctants via the identification $N - k_r = k_r$ for $k_r = 1, \dots, \frac{N}{2} - 1$ and $r = 1, \dots, d$.

In (56), α is the decay exponent of the spectral energy in the Fourier basis. The dependence of the prefactor on N is arbitrary as far as scaling exponents are concerned, as any prefactor will cancel out in (44). The particular choice made in (56) is such that $\mathbb{E}E_n$ converges to a finite positive value while $\operatorname{Var} E_n$ goes to zero as $n \to \infty$, as we shall show below. Our main result can be stated as follows.

Theorem 4.1. *In the setting described above, for every fixed $\ell \in \mathbb{N}_0$,*

$$\mathbb{E}E_{n-\ell} \to \begin{cases} \displaystyle\int_{[0,1/2]^d} \frac{\bigl(1-\prod_{r=1}^d \cos^2(2^\ell \pi x_r)\bigr)\,\prod_{p=1}^\ell \prod_{r=1}^d \cos^2(2^{p-1}\pi x_r)}{|\boldsymbol{x}|^{-\alpha+d-1}}\,\mathrm{d}\boldsymbol{x} & \text{for } \alpha > -3 \\ C\,4^\ell & \text{for } \alpha < -3 \end{cases} \tag{57}$$

as $N = 2^n \to \infty$, where

$$C = \pi^2 \sum_{\boldsymbol{k}\in\mathbb{Z}^d} |\boldsymbol{k}|^{\alpha-d+3} < \infty. \tag{58}$$

Moreover, $\operatorname{Var} E_{n-\ell} \to 0$ *as $N = 2^n \to \infty$.*

Proof. The averaging operator $\mathcal{A}_N \colon \mathscr{L}_N \to \mathscr{L}_{N/2}$ introduced in Section 4.2 acts on basis functions according to

$$\begin{aligned} \mathcal{A}_N f_{N,\boldsymbol{k}}(\boldsymbol{x}) &= \exp(2\pi \mathrm{i}\boldsymbol{k}\cdot\boldsymbol{x})\,2^{-d} \sum_{\boldsymbol{e}\in\{0,1\}^d} \exp\Bigl(\frac{2\pi\mathrm{i}\boldsymbol{k}\cdot\boldsymbol{e}}{N}\Bigr) \\ &= \varphi_N(\boldsymbol{k})\, f_{N/2,\boldsymbol{k} \bmod N/2}(\boldsymbol{x}) \end{aligned} \tag{59}$$

for $\boldsymbol{x} \in \mathbb{Z}_N^d/(N/2)$ and $\boldsymbol{k} \in \mathbb{Z}_N^d$, where

$$\varphi_N(\boldsymbol{k}) = \exp\Bigl(\frac{\pi\mathrm{i}\boldsymbol{k}\cdot\boldsymbol{1}}{N}\Bigr) \prod_{r=1}^d \cos\Bigl(\frac{\pi k_r}{N}\Bigr) \tag{60}$$

with $\boldsymbol{1} = (1,\dots,1)$. For a general function u with Fourier expansion (55), we have

$$\mathcal{A}_N u = \sum_{\boldsymbol{k}\in\mathbb{Z}^d_{N/2}} f_{\frac{N}{2},\boldsymbol{k}} \sum_{\boldsymbol{e}\in\{0,1\}^d} \varphi_N(\boldsymbol{k}+\tfrac{N}{2}\boldsymbol{e})\, u_{\boldsymbol{k}+\frac{N}{2}\boldsymbol{e}}, \tag{61}$$

and the corresponding energy is

$$\|\mathcal{A}_N u\|^2_{N/2} = \sum_{\boldsymbol{k}\in\mathbb{Z}^d_{N/2}} \sum_{\boldsymbol{e},\boldsymbol{e}'\in\{0,1\}^d} \varphi_N(\boldsymbol{k}+\tfrac{N}{2}\boldsymbol{e})\,\varphi_N^*(\boldsymbol{k}+\tfrac{N}{2}\boldsymbol{e}')\, u_{\boldsymbol{k}+\frac{N}{2}\boldsymbol{e}}\, u^*_{\boldsymbol{k}+\frac{N}{2}\boldsymbol{e}'}. \tag{62}$$

When $\frac{N}{2}$ is even, we can iterate the averaging operator and obtain

$$\mathcal{A}_{\frac{N}{2}}\mathcal{A}_N u = \sum_{\boldsymbol{k}\in\mathbb{Z}^d_{N/4}} f_{\frac{N}{4},\boldsymbol{k}} \sum_{\boldsymbol{e},\boldsymbol{g}\in\{0,1\}^d} \varphi_{\frac{N}{2}}(\boldsymbol{k}+\tfrac{N}{4}\boldsymbol{g})\,\varphi_N(\boldsymbol{k}+\tfrac{N}{2}\boldsymbol{e}+\tfrac{N}{4}\boldsymbol{g})\, u_{\boldsymbol{k}+\frac{N}{2}\boldsymbol{e}+\frac{N}{4}\boldsymbol{g}}, \tag{63}$$

with corresponding energy

$$\begin{aligned} \|\mathcal{A}_{\frac{N}{2}}\mathcal{A}_N u\|^2_{N/4} = \sum_{\boldsymbol{k}\in\mathbb{Z}^d_{N_2}} \sum_{\boldsymbol{e},\boldsymbol{g},\boldsymbol{e}',\boldsymbol{g}'\in\{0,1\}^d} & \varphi_{\frac{N}{2}}(\boldsymbol{k}+\tfrac{N}{4}\boldsymbol{g})\,\varphi^*_{\frac{N}{2}}(\boldsymbol{k}+\tfrac{N}{4}\boldsymbol{g}') \\ & \cdot \varphi_N(\boldsymbol{k}+\tfrac{N}{2}\boldsymbol{e}+\tfrac{N}{4}\boldsymbol{g})\,\varphi_N^*(\boldsymbol{k}+\tfrac{N}{2}\boldsymbol{e}'+\tfrac{N}{4}\boldsymbol{g}')\, u_{\boldsymbol{k}+\frac{N}{2}\boldsymbol{e}+\frac{N}{4}\boldsymbol{g}}\, u^*_{\boldsymbol{k}+\frac{N}{2}\boldsymbol{e}'+\frac{N}{4}\boldsymbol{g}'}. \end{aligned} \tag{64}$$

These expressions imply that, when the $u_{\boldsymbol{k}} = \sigma_{\boldsymbol{k}}\,\zeta_{\boldsymbol{k}}$ are independent random variables, that

$$\mathbb{E}\|u\|_N^2 = \sum_{\boldsymbol{k}\in\mathbb{Z}_N^d} \sigma_{\boldsymbol{k}}^2, \tag{65a}$$

$$\mathbb{E}\|\mathcal{A}_N u\|_{N/2}^2 = \sum_{\boldsymbol{k}\in\mathbb{Z}_N^d} |\varphi_N(\boldsymbol{k})|^2\,\sigma_{\boldsymbol{k}}^2, \tag{65b}$$

$$\begin{aligned}\mathbb{E}\|\mathcal{A}_{\frac{N}{2}}\mathcal{A}_N u\|_{N/4}^2 &= \sum_{\boldsymbol{k}\in\mathbb{Z}_N^d} |\varphi_{\frac{N}{2}}(\boldsymbol{k} \bmod \tfrac{N}{2})\,\varphi_N(\boldsymbol{k})|^2\,\sigma_{\boldsymbol{k}}^2 \\ &= \sum_{\boldsymbol{k}\in\mathbb{Z}_N^d} |\varphi_{\frac{N}{2}}(\boldsymbol{k})\,\varphi_N(\boldsymbol{k})|^2\,\sigma_{\boldsymbol{k}}^2 \end{aligned} \tag{65c}$$

and, in general,

$$\mathbb{E}\|\mathcal{A}_{2^{-\ell}N}\dots\mathcal{A}_N u\|_{2^{-\ell-1}N}^2 = \sum_{\boldsymbol{k}\in\mathbb{Z}_N^d} \sigma_{\boldsymbol{k}}^2 \prod_{i=0}^{\ell} |\varphi_{2^{-i}N}(\boldsymbol{k})|^2. \tag{66}$$

Inserting our stochastic model (56), we need to distinguish two cases. First, when $\alpha > -3$, we can view the expressions in (65) as Riemann sum approximations of the corresponding integrals, so that, referring to the definition of E_ℓ in (42),

$$\begin{aligned}\mathbb{E}E_n &= \Big(\frac{1}{N}\Big)^d \sum_{\boldsymbol{k}\in\mathbb{Z}_{N/2}^d} \bigg(1 - \prod_{r=1}^d \cos^2\Big(\frac{\pi k_r}{N}\Big)\bigg) \Big(\frac{|\boldsymbol{k}|}{N}\Big)^{\alpha-d+1} \\ &\to \int_{[0,1/2]^d} \frac{1 - \prod_{r=1}^d \cos^2(\pi x_r)}{|\boldsymbol{x}|^{-\alpha+d-1}}\,\mathrm{d}\boldsymbol{x}, \end{aligned} \tag{67}$$

as $N\to\infty$, and likewise

$$\begin{aligned}\mathbb{E}E_{n-1} &= \Big(\frac{1}{N}\Big)^d \sum_{\boldsymbol{k}\in\mathbb{Z}_{N/2}^d} \bigg(1 - \prod_{r=1}^d \cos^2\Big(\frac{2\pi k_r}{N}\Big)\bigg) \prod_{r=1}^d \cos^2\Big(\frac{\pi k_r}{N}\Big) \Big(\frac{|\boldsymbol{k}|}{N}\Big)^{\alpha-d+1} \\ &\to \int_{[0,1/2]^d} \frac{\big(1 - \prod_{r=1}^d \cos^2(2\pi x_r)\big)\,\prod_{r=1}^d \cos^2(\pi x_r)}{|\boldsymbol{x}|^{-\alpha+d-1}}\,\mathrm{d}\boldsymbol{x}. \end{aligned} \tag{68}$$

Iterating this process, we obtain the first case of statement (57).

Next, we prove that $\operatorname{Var} E_{n-\ell} \to 0$ for $\ell = 0, 1$. Let us focus on the case $\ell = 0$, the general case is similar. The first step is to decompose E_n as the sum of independent terms:

$$E_n = \|u\|_N^2 - \|\mathcal{A}_N u\|_{N/2}^2 = \sum_{\boldsymbol{k}\in\mathbb{Z}_{N/2}^d} e(\boldsymbol{k}) \tag{69}$$

with

$$e(\boldsymbol{k}) = \sum_{\boldsymbol{e},\boldsymbol{e}' \in \{0,1\}^d} \left(\delta_{\boldsymbol{e},\boldsymbol{e}'} - \varphi_N(\boldsymbol{k} + \tfrac{N}{2}\boldsymbol{e})\, \varphi_N^*(\boldsymbol{k} + \tfrac{N}{2}\boldsymbol{e}')\right) u_{\boldsymbol{k}+\frac{N}{2}\boldsymbol{e}}\, u^*_{\boldsymbol{k}+\frac{N}{2}\boldsymbol{e}'}. \tag{70}$$

All $e(\boldsymbol{k})$ are independent with mean

$$\mathbb{E}e(\boldsymbol{k}) = \sum_{\boldsymbol{e} \in \{0,1\}^d} (1 - |\varphi_N(\boldsymbol{k} + \tfrac{N}{2}\boldsymbol{e})|^2)\, \sigma^2_{\boldsymbol{k}+\frac{N}{2}\boldsymbol{e}}. \tag{71}$$

To compute the variance, we note that

$$\begin{aligned} e^2(\boldsymbol{k}) = \sum_{\boldsymbol{e}_1,\boldsymbol{e}_2,\boldsymbol{e}_3,\boldsymbol{e}_4 \in \{0,1\}^d} & \left(\delta_{\boldsymbol{e}_1,\boldsymbol{e}_2} - \varphi_N(\boldsymbol{k} + \tfrac{N}{2}\boldsymbol{e}_1)\, \varphi_N^*(\boldsymbol{k} + \tfrac{N}{2}\boldsymbol{e}_2)\right) \\ & \cdot \left(\delta_{\boldsymbol{e}_3,\boldsymbol{e}_4} - \varphi_N(\boldsymbol{k} + \tfrac{N}{2}\boldsymbol{e}_3)\, \varphi_N^*(\boldsymbol{k} + \tfrac{N}{2}\boldsymbol{e}_4)\right) \cdot u_{\boldsymbol{k}+\frac{N}{2}\boldsymbol{e}_1}\, u^*_{\boldsymbol{k}+\frac{N}{2}\boldsymbol{e}_2}\, u_{\boldsymbol{k}+\frac{N}{2}\boldsymbol{e}_3}\, u^*_{\boldsymbol{k}+\frac{N}{2}\boldsymbol{e}_4}. \end{aligned} \tag{72}$$

Using (71) and (72), we deduce that

$$\begin{aligned} \operatorname{Var} e(\boldsymbol{k}) = \mathbb{E}e^2(\boldsymbol{k}) - (\mathbb{E}e(\boldsymbol{k}))^2 = & \sum_{\boldsymbol{e} \in \{0,1\}^d} \left(1 - |\varphi_N(\boldsymbol{k} + \tfrac{N}{2}\boldsymbol{e})|^2\right)^2 \sigma^4_{\boldsymbol{k}+\frac{N}{2}\boldsymbol{e}}\, \mathbb{E}(\zeta^4_{\boldsymbol{k}} - 1) \\ + \sum_{\boldsymbol{e}_1 \neq \boldsymbol{e}_2} & \left(|\varphi_N(\boldsymbol{k} + \tfrac{N}{2}\boldsymbol{e}_1)\, \varphi_N(\boldsymbol{k} + \tfrac{N}{2}\boldsymbol{e}_2)|^2 + \varphi_N(\boldsymbol{k} + \tfrac{N}{2}\boldsymbol{e}_1)^2\, \varphi_N^*(\boldsymbol{k} + \tfrac{N}{2}\boldsymbol{e}_2)^2\right) \sigma^2_{\boldsymbol{k}+\frac{N}{2}\boldsymbol{e}_1}\, \sigma^2_{\boldsymbol{k}+\frac{N}{2}\boldsymbol{e}_2} \end{aligned} \tag{73}$$

where, by assumption, the $\mathbb{E}\zeta^4_{\boldsymbol{k}}$ are identical and finite. We distinguish two cases. When $\alpha - d + 1 \geq 0$, summing up the independent variances (73) gives a Riemann sum similar to (67) and (68), but multiplied with an additional factor N^{-d} since the power on the $\sigma_{\boldsymbol{k}}$ is 4, not 2. Thus, $\operatorname{Var} E_n \to 0$ as $n \to \infty$. When $\alpha - d + 1 < 0$, the upper bound is more subtle. The worst-case term in the first sum of (73) is when $\boldsymbol{e} = 0$, so the largest term is bounded by $(|\boldsymbol{k}|/N)^4 \sigma^4_{\boldsymbol{k}}$ up to a constant factor. The worst-case terms in the second sum of (73) is when $\boldsymbol{e}_1 = 0$ and $\boldsymbol{e}_2$ has only one non-zero component, or vice versa. In that case, exactly one of the cosine prefactors is shifted to a sine, and we obtain an upper bound of the form $(|\boldsymbol{k}|/N)^2\, \sigma^2_{\boldsymbol{k}}\, N^{-d}$ up to a constant factor, which is smaller than the contribution from the first sum.

In conclusion, summing up these bounds over all contributing wave numbers and using an integral upper bound, we obtain

$$\begin{aligned} \operatorname{Var} E_n &\leq \frac{C_1}{N^d} \int_{\frac{1}{N} < |\boldsymbol{x}| < 1} |\boldsymbol{x}|^{4\beta+4}\, \mathrm{d}\boldsymbol{x} \\ &\leq \frac{C_2}{N^d} \int_{\frac{1}{N}}^1 x^{4\beta+4}\, x^{d-1}\, \mathrm{d}x \\ &= O(N^{-2\alpha-6}) \to 0 \end{aligned} \tag{74}$$

since $\alpha > -3$.

We now turn to the case $\alpha < -3$. Now, the integral used in (67) is no longer a valid limit of the corresponding Riemann sum—in fact, it diverges near $\boldsymbol{k} = 0$—and we have to work with the sum directly. Fixing $\gamma \in (0,1)$, we split the sum as follows:

$$\begin{aligned}
\mathbb{E}E_n &= N^2 \sum_{\boldsymbol{k}\in\mathbb{Z}^d_{N/2}} \Bigl(1 - \prod_{r=1}^{d} \cos^2\Bigl(\frac{\pi k_r}{N}\Bigr)\Bigr) |\boldsymbol{k}|^{\alpha-d+1} \\
&= N^2 \sum_{\substack{\boldsymbol{k}\in\mathbb{Z}^d_{N/2} \\ |\boldsymbol{k}|\le N^\gamma}} \Bigl(1 - \prod_{r=1}^{d} \cos^2\Bigl(\frac{\pi k_r}{N}\Bigr)\Bigr) |\boldsymbol{k}|^{\alpha-d+1} + N^2 \sum_{\substack{\boldsymbol{k}\in\mathbb{Z}^d_{N/2} \\ |\boldsymbol{k}|> N^\gamma}} \Bigl(1 - \prod_{r=1}^{d} \cos^2\Bigl(\frac{\pi k_r}{N}\Bigr)\Bigr) |\boldsymbol{k}|^{\alpha-d+1} \\
&= C + o(1) + O(N^{2+\gamma(\alpha+1)}),
\end{aligned} \tag{75}$$

where C is given by (58). To see that the first sum in the second line of (75) equals $C+o(1)$, we only need to observe that $1 - \cos^2 x = x^2 + o(x^2)$. For the second sum, we bound the term in parentheses by 2, then estimate the resulting expression with an integral. This last contribution is subdominant if $2 + \gamma(\alpha+1) < 0$, or $\gamma > \frac{-2}{\alpha+1}$. The resulting lower bound on γ is consistent with the requirement that $\gamma < 1$ for every $\alpha < -3$.

Applying the same arguments to $E_{n-\ell}$ for some fixed $\ell = 1, 2, \dots$, we find that, for $\alpha < -3$,

$$\mathbb{E}E_{n-\ell} = 4^\ell\, C + o(1). \tag{76}$$

The proof that the variances of $E_{n-\ell}$ vanish is similar to the proof in the first case, we omit all details. □

Referring to the discussion and notation introduced at the end of Section 4.2, we immediately obtain the following result on the derived spectral slopes.

Corollary 4.2. *Under the conditions of Theorem 4.1,* $\alpha_{\mathrm{c}}^{\mathrm{WR}}(n-\ell) \to -3$ *if* $\alpha \le -3$ *and*

$$\alpha_{\mathrm{c}}^{\mathrm{WR}}(n-\ell) \to -1 + \log_2 \frac{\displaystyle\int_{[0,1/2]^d} \frac{\bigl(1 - \prod_{r=1}^{d} \cos^2(2^\ell \pi x_r)\bigr) \prod_{p=1}^{\ell} \prod_{r=1}^{d} \cos^2(2^{p-1}\pi x_r)}{|\boldsymbol{x}|^{-\alpha+d-1}} \,\mathrm{d}\boldsymbol{x}}{\displaystyle\int_{[0,1/2]^d} \frac{\bigl(1 - \prod_{r=1}^{d} \cos^2(2^{\ell+1} \pi x_r)\bigr) \prod_{p=1}^{\ell+1} \prod_{r=1}^{d} \cos^2(2^{p-1}\pi x_r)}{|\boldsymbol{x}|^{-\alpha+d-1}} \,\mathrm{d}\boldsymbol{x}} \tag{77}$$

otherwise, in probability as $N = 2^n \to \infty$ *with* $\ell \in \mathbb{N}_0$ *fixed. In* (77)*, read* $\prod_a^b = 1$ *when* $b < a$.

Proof. Equation (77) is obtained by substituting (57) into (45) and applying the argument stated below (46). □

Remark 4.3. Formula (1) quoted in the introduction is the special case of this corollary when $\ell = 0$.

Remark 4.4. The case $\alpha = -3$ is special, since $C = +\infty$ in (58). Thus, Theorem 4.1 as stated does not hold when $\alpha = -3$ due to the particular choice of scaling in (56). However, the ratio $\mathbb{E}E_{n-\ell}/\mathbb{E}E_{n-\ell-1}$ remains well-defined as $\alpha \to -3$, so that the corollary holds true for all values of α. In particular, the choice of prefactors in (56) has no impact on the corollary: We may simply assume $\sigma_{\boldsymbol{k}} = |\boldsymbol{k}|^{\frac{\alpha-d+1}{2}}$ and (77) will remain true.

Remark 4.5. With substantially more effort, it is possible to obtain results as in Section 4.3, namely that, under appropriate central limit theorem scaling, the difference between LHS and RHS in (77) converges in distribution to a Gaussian. However, the precise parameters and conditions are too complicated for practical use.

Remark 4.6. It is always possible to use the sum expressions in the first line of (67), (68), and the corresponding generalizations in place of the Riemann sum approximations stated in Theorem 4.1 and its corollary. However, the integral expressions are more convenient to work with and the approximation error is typically small compared to the statistical variance.

The results of the theorem are demonstrated in Fig. 3. It can be seen that for the large scales, where fewer coefficients contribute to each spectral band, the variance of the spectral density and its derivative increases. The data for small scales almost coincides with the expected values. The analytical expressions for the expected values allow us to apply corrections to the computed data, which, in turn, allows us to recover the slope with respect to the Fourier basis with high probability, see Fig. 4.

Remark 4.7. We have provided a detailed analysis of WR-diagnostics applied to data prepared in the F-basis. A converse analysis is also possible, as shown in Fig. 5. The original slopes are drawn by solid lines, the dots are related to the F-diagnostics. The setup on the WR-side is essentially described by (47) extended to all scales. It is seen that the WR-slopes are close to the diagnosed F-slopes so long as the WR-slopes are more shallow than approximately -2. We observe that the threshold for F-diagnostics of WR-fields is more restrictive than in the forward case we focused on. The reason is the following: The WR-spectral energy density for simple Fourier harmonics scales like k^{-3}, see (2), while F-spectral energy density for a single step function scales like k^{-2}, as an easy explicit computation shows. Note that there is step-like behavior in the assignment of the amplitudes of the WR-coefficients because – as explained earlier – there is no natural internal ordering within each integer-indexed wavenumber shell. The corresponding F-spectrum, however, appears smoother as the F-transform of a WR-basis function is spread out in wavenumber space.

5. Examples

In the following, we illustrate the main points of this paper with concrete examples. We start with the deterministic case to support the observations presented in Section 3. These idealized cases show that both diagnostics, whether based on the Fourier or the Walsh–Rademacher basis, provide similar qualitative spectral analysis. This qualitative agreement

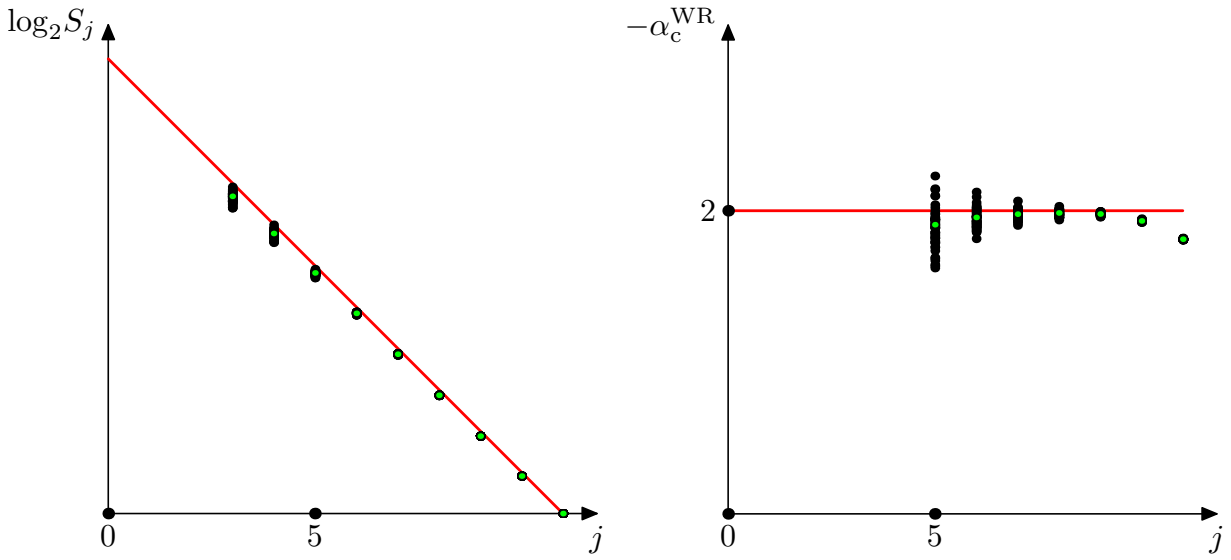

(a) spectral density

(b) its derivative

Figure 3: The logarithmic spectral density $\log_2 S_j$ (the vertical axis is shifted such that the last point lies on the horizontal axis) and its derivative $\alpha_{\mathrm{c}}^{\mathrm{WR}}$, see (44), are shown by black points. Each of the quantities computed for 50 (100 for both) independently and randomly generated fields on the mesh of the size $N = 2048$ with $\alpha = -2$. The red line indicates the exact slope α and $-\alpha$, respectively, the green points show analytic results $\log_2 S^{\mathrm{e}}(j) \equiv \log_2(2^{-j}\mathbb{E}E_j)$, see (43) and (57), and $\alpha_{\mathrm{e}}^{\mathrm{WR}}$ denoting the right hand side of (77), where the integrals are computed by a Riemann sum approximation with step size $1/2048$.

is very important and justifies the use of both methods for diagnostics for practical purposes, as was done in our analysis of zonal channel flow, see [14]. We then turn to statistical analysis, highlighting the more subtle quantitative differences between F- and WR-diagnostics in the discrete case as presented in Section 4.

5.1. Simple harmonics

We consider the rhombus Ω generated by the vectors $(1, 0)$ and $(1/2, \sqrt{3}/2)$, cf. (17). We analyze the function

$$u(x, y) = \cos\Big(2\pi \cdot 3x + \frac{4\pi \cdot 2y}{\sqrt{3}}\Big) \tag{78}$$

which, up to a multiplicative constant, coincides with one of the Fourier basis functions (18). We consider the cumulative spectral energy computed with respect to three different scale decompositions. The first is $E^{\mathrm{F}}_{[0,k)}$ computed via the Fourier scale decomposition, see (20). The second one is

$$E^{\mathrm{DIAMOND}}_{[0,k)} = \int_0^k \|\hat{u}(k)\|^2 \,\mathrm{d}\mu, \tag{79}$$

see (26), corresponding to the Walsh–Rademacher scale decomposition on a uniform diamond mesh partition, where each rhombus A_{c} is similar to Ω. The third, $E^{\mathrm{TRIANGLE}}_{[0,k)}$, uses the Walsh–Rademacher scale decomposition on the same mesh, but with each rhombus divided into two triangles.

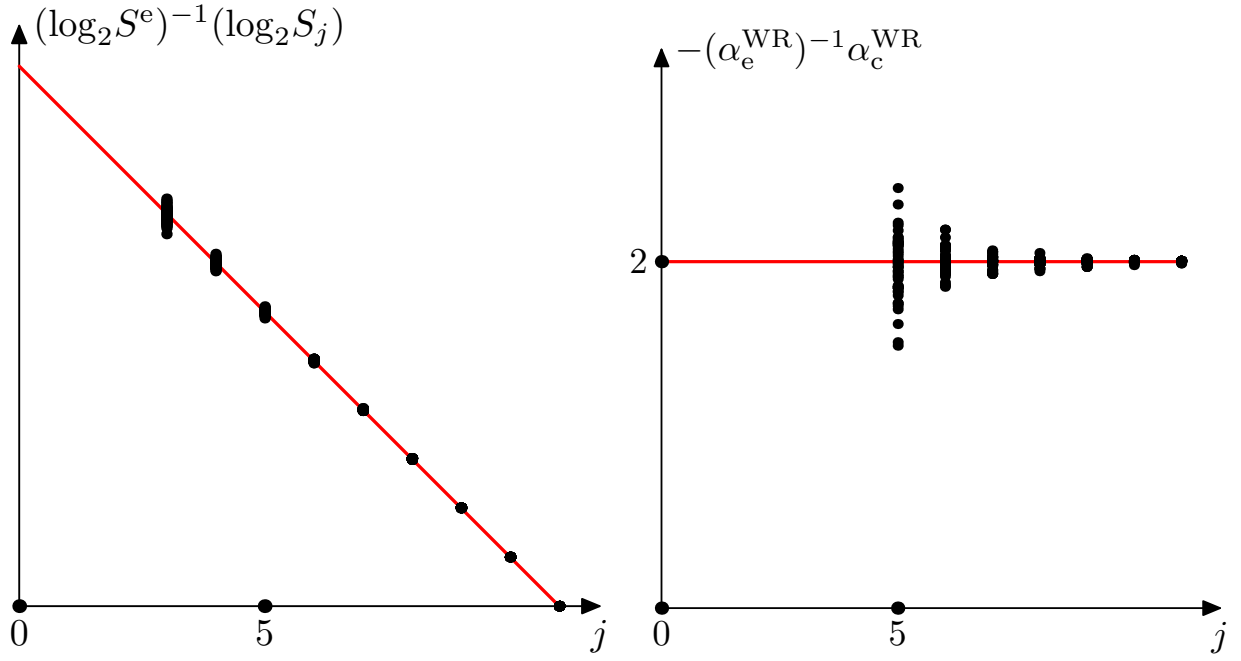

(a) corrected spectral density

(b) corrected derivative

Figure 4: In the same setup as in Fig. 3, the corrected spectral density and its derivative are plotted. The correction is the application of inverse functions of $\log_2 S^{\mathrm{e}}$ and $\alpha_{\mathrm{e}}^{\mathrm{WR}}$, available analytically, to the corresponding computed data.

The partition of Ω into one uniform rhombus (itself) corresponds to $k = \sqrt{2}$, into four uniform rhombuses to $k = 2\sqrt{2}$, and so on. Thus, $E^{\mathrm{DIAMOND}}_{[0,k)}$ is defined at $k = 2^{n-\frac{1}{2}}$, $n \in \mathbb{N}$. Similarly, the partition of Ω into two uniform triangles corresponds to $k = 2$, into eight uniform triangles to $k = 4$, and so on. Thus, $E^{\mathrm{TRIANGLE}}_{[0,k)}$ is defined at $k = 2^n$, $n \in \mathbb{N}$. The difference between the wavenumbers on triangular and diamond meshes is natural, since 2 triangles form 1 rhombus and, hence, two triangles resolve $2^{1/d}$ more scales than one rhombus, where $d = 2$ is the dimension of the domain Ω.

Moreover, both E^{TRIANGLE} and E^{DIAMOND} are monotonic functions, since they correspond to nested partitions. Also, by the same reasons $E^{\mathrm{DIAMOND}}_{[0,k)} \leq E^{\mathrm{TRIANGLE}}_{[0,k\sqrt{2})}$.

In Fig. 6, we compare the cumulative energies $E^{\mathrm{F}}_{[0,k)}$ (black points), $E^{\mathrm{DIAMOND}}_{[0,k)}$ (blue points) and $E^{\mathrm{TRIANGLE}}_{[0,k)}$ (red points). The corresponding asymptotic expression (28) with the quadratic forms defined by (34) (thin blue line) and (36) (thin red line) are also shown. The agreement of the asymptotic expression with the exact value for finite k is rather good even for moderate values of k. We also see qualitative agreement, even though the step function corresponding to the Fourier basis is spread out over several scale intervals in the Walsh–Rademacher basis.

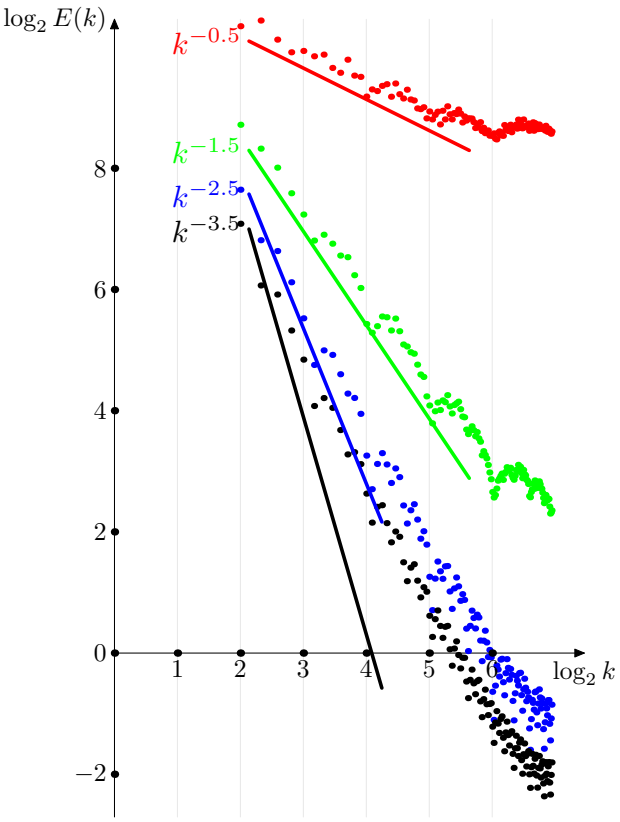

Figure 5: F-diagnostics of WR-slopes -0.5 (red), -1.5 (green), -2.5 (blue), -3.5 (black). Original slopes in WR-basis are presented by solid lines, their F-diagnostics are dots. 2000 random WR-fields at resolution 256×256 are generated for each of the slopes, then the average of all the F-diagnostics is taken.

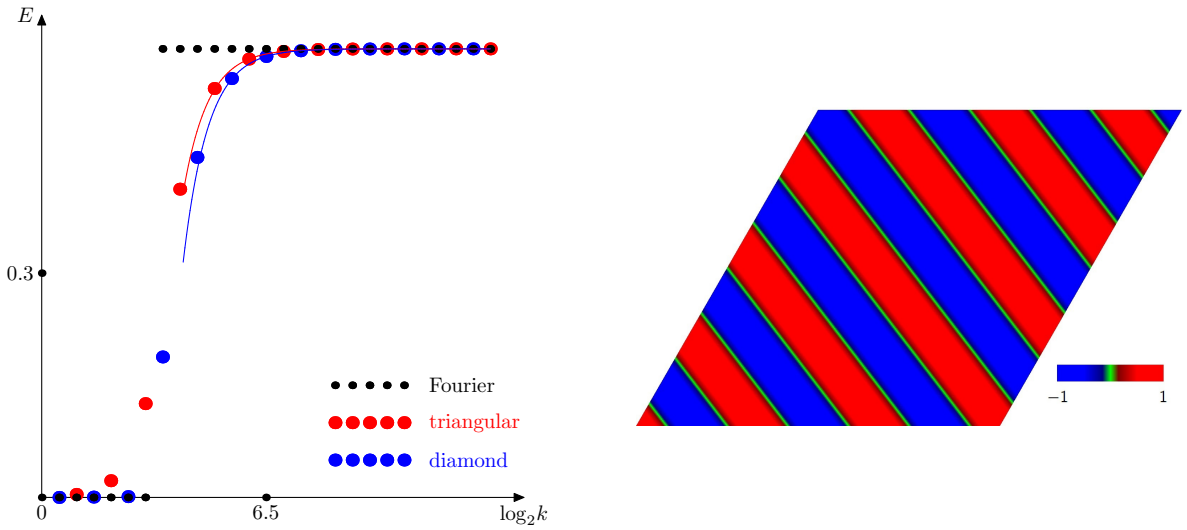

Figure 6: Cumulative spectral energy for one harmonic (78), shown on the right within one unit cell of the diamond mesh. Red dots: triangular mesh, blue dots: diamond mesh, black dots: Fourier basis. The thin lines show the asymptotic expression (28) with the quadratic forms defined by (34) resp. (36).

5.2. Wave field

The next example is a superposition of Fourier harmonics with a k^{-2} power law up to a maximum wave number of $k_i = 64$,

$$u(x,y,t) = \sum_{\substack{n,m=0 \\ n^2+m^2\neq 0}}^{64,64} \frac{\cos\Big(2\sqrt{n^2+\frac{4m^2}{3}}\,\pi t\Big)}{(n^2+m^2+1)^{\frac{1}{4}}}\,\cos\Big(2\pi\cdot nx + \frac{4\pi\cdot my}{\sqrt{3}}\Big). \tag{80}$$

This function describes a wave field which is the solution of the linear wave equation

$$\frac{\partial^2 u}{\partial x^2} + \frac{\partial^2 u}{\partial y^2} = \frac{\partial^2 u}{\partial t^2}. \tag{81}$$

We observe good agreement between the spectral analysis in the different bases. In particular, the results of the Walsh–Rademcher analysis do not depend on time t even though the wave pattern in physical space is very different near time $t = 0$ (Fig. 7) and much later times (Fig. 8). Note that in this example the "energies" shown are different from the physical notion of energy for the wave propagation problem.

5.3. Statistical analysis

The evolution of a wave field with non-commensurate frequencies in the previous section already has characteristics of a pseudo-random field. We now move to the fully random setting analyzed in Section 4.

We take a square mesh in $d = 2$ dimensions and generate an ensemble of random fields having a spectral slope α (i) in the Walsh–Rademacher basis, see (47), and (ii) in the Fourier basis, see (56). In both cases, we diagnose the spectral slope $\alpha_{\mathrm{c}}^{\mathrm{WR}}$ with respect to the Walsh–Rademacher basis, see (44). Fig. 9 shows results for a 100×100 mesh, 40 random field samples for each α, and 400 different values of α in the interval $-\alpha \in [-1, 4]$. As expected, α is well recovered when the spectral slope of the random field is also prepared in the Walsh–Rademacher basis (Fig. 9 left). In our example, we use random variables uniformly distributed on $[-b, b]$ for some $b > 0$. Hence, the corresponding moments are $(D_4 - D_2^2)/D_2^2 = (b^4/5 - b^4/9)/(b^4/9) = 4/5$, so that the variance in (52) is

$$N\sigma = \sqrt{\frac{(D_4 - D_2^2)\,(4^d + 2^d)}{(D_2 \ln 2)^2\,(2^d - 1)}} = \sqrt{\frac{4\,(16+4)}{5\,(\ln 2)^2\,3}} = \frac{4}{\sqrt{3}\,\ln 2}. \tag{82}$$

Thus, the variance of the diagnosed spectral slope is very small for typical values of N, as confirmed by the numerical experiment.

The situation is more complicated when the spectral slope of the random field is prepared in the Fourier basis, see Fig. 9 (middle). As expected, the diagnosed spectral slope $\alpha_{\mathrm{c}}^{\mathrm{WR}}$ is different from α and scatters around the expected spectral slope $\alpha_{\mathrm{e}}^{\mathrm{WR}}$, drawn in green. Note that the distribution of the $\alpha_{\mathrm{c}}^{\mathrm{WR}}$ for finite N is not symmetric as we always have $\alpha_{\mathrm{c}}^{\mathrm{WR}} > -3$, even though it is asymptotically normal as $N \to \infty$.

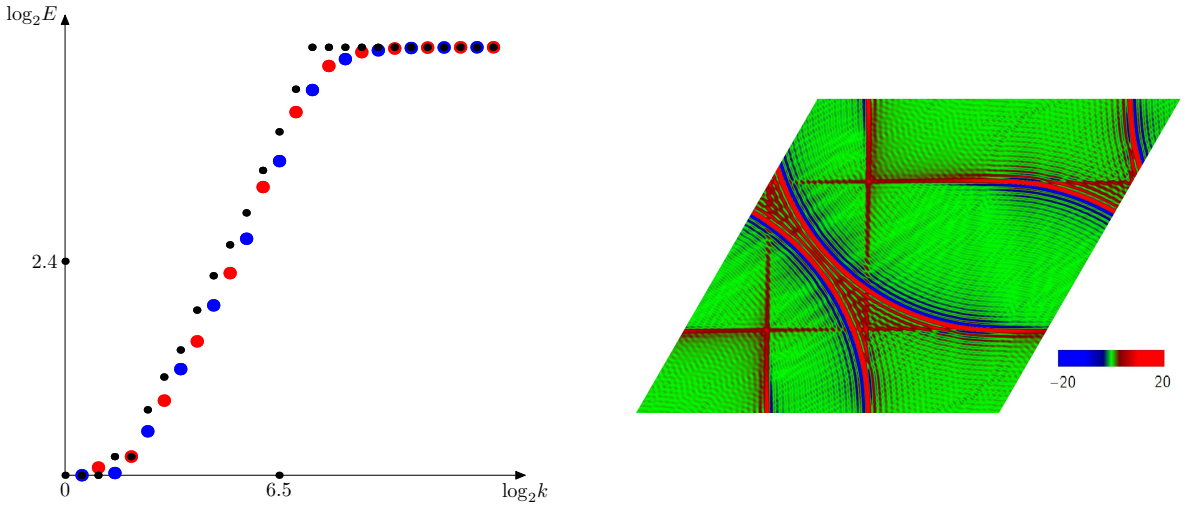

Figure 7: Wave field u at $2\pi t = 4$, see (80). For the legend see Fig. 6.

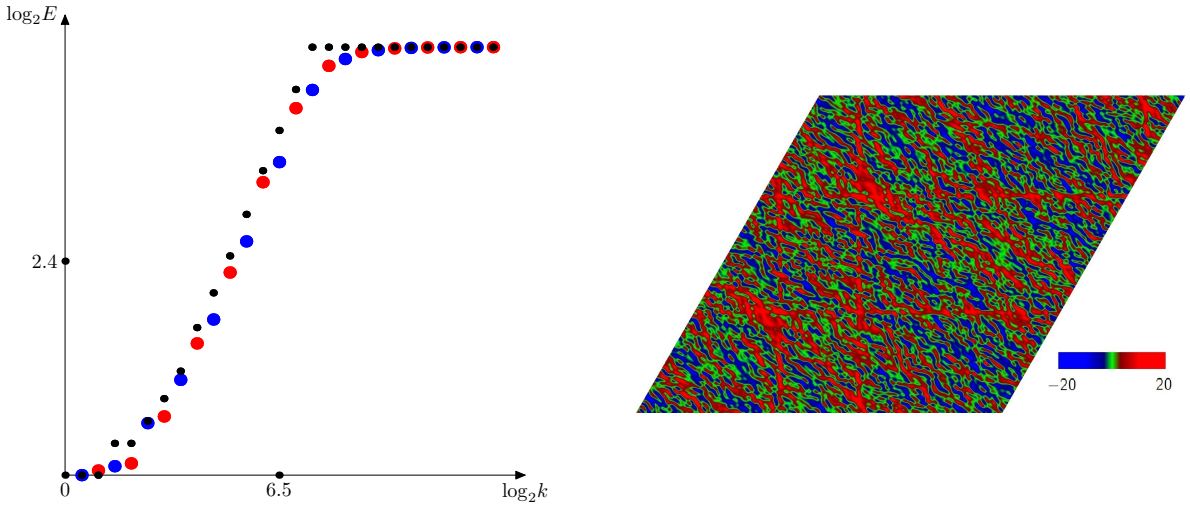

Figure 8: Wave field u at $2\pi t = 154300$, see (80). For the legend see Fig. 6.

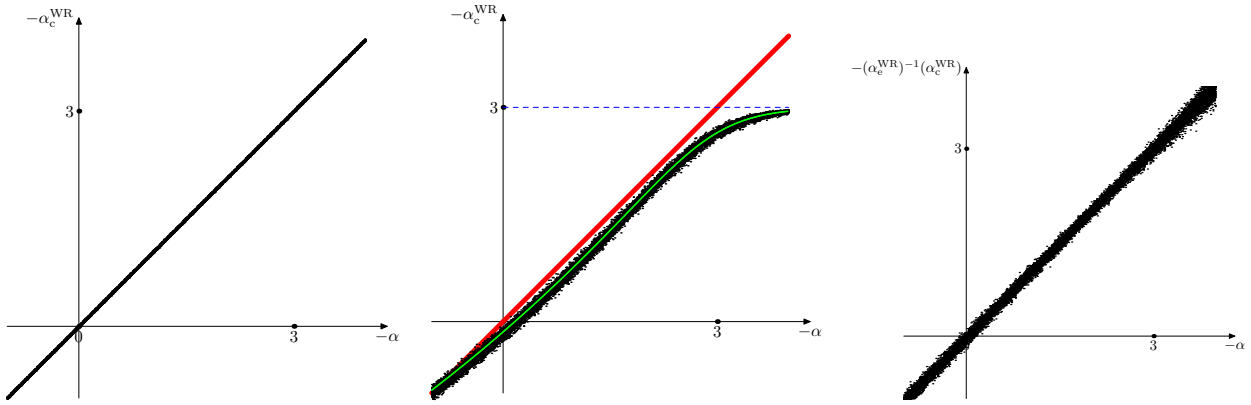

Figure 9: Diagnosed spectral slope α_c^{WR} when the random field is prepared with spectral slope α in the Walsh–Rademacher basis (left) and in the Fourier basis (middle). The red line corresponds to $\alpha_c^{WR} = \alpha$, plotted for orientiation. The green curve is the expected spectral slope α_e^{WR}. The right panel shows the corrected spectral slope diagnosed in the Walsh–Rademacher basis, using the analytic dependency between Walsh–Rademacher and Fourier basis as correction factor.

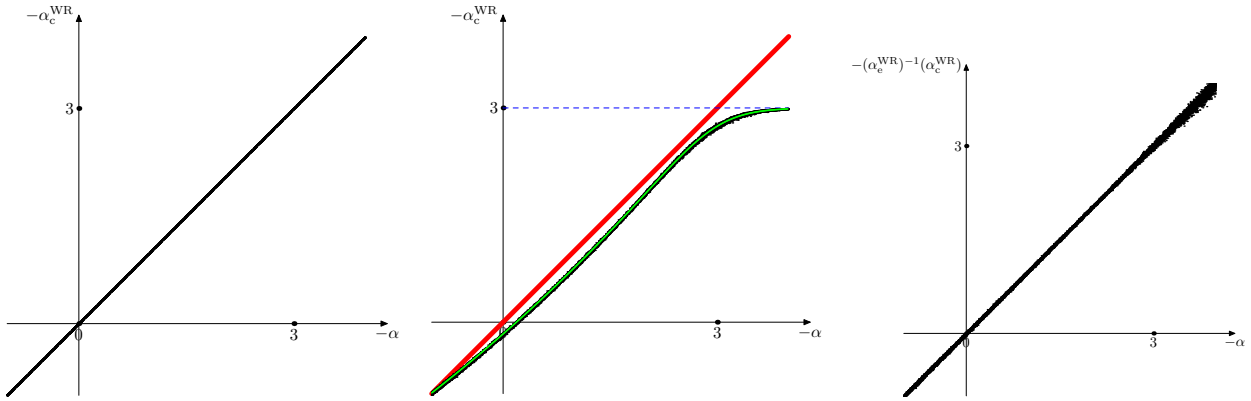

Figure 10: The same setup as in Fig. 9 but with the mesh size $N = 400$ instead of $N = 100$.

We note that the integral approximation to α_e^{WR} stated in (77) and the exact value of α_e^{WR} are practically identical for $\alpha \in [-2.7, 0]$ and $N \geq 100$. While the integral approximation is more convenient for some analytical statements, the exact value of α_e^{WR} is easily computed and can be used to correct the diagnosed spectral slope α_c^{WR} to get a better estimate for α, see Fig. 9 (right). Since α_e^{WR} is asymptotic to -3, the recovery is increasingly ill-conditioned for $\alpha < -3$. However, given enough realizations, recovery is still possible.

In Fig. 10, we show the analog of Fig. 9 (middle) for $N = 400$ instead of $N = 100$.

6. Conclusion

The resize-and-average method provides a simple computational method to estimate spectra on arbitrary nested meshes. In general, the Walsh–Rademacher spectra obtained this way differ from spectra relative to other bases, in particular to the discrete Fourier basis. However, we have shown that, in a statistical sense, we can compensate for this discrepancy,

on finite meshes even for spectra somewhat steeper than k^{-3}, the natural limiting case for step-function-based methods on the continuum.

In this work, we have derived the correction factor analytically for a regular mesh. For unstructured meshes, the correction factor can be determined computationally by doing statistics over a large number of realizations of the random field. In this more general case, a hierarchy of meshes may be constructed via membership of cells or cell centers in an overlay dyadic grid. This auxiliary grid is only used to structure the analysis grid, but no interpolation onto the dyadic grid is performed [14].

In principle, the analysis performed here can also be applied to the reverse problem: diagnosing the spectral slope of a WR-random field in the Fourier basis. Numerical experiments, see Remark 4.7, indicate that the behavior is similar to that of our main case, namely diagnosing F-random fields in the WR-basis. We refrain from providing details for two reasons. First, explicit expressions appear possible, but cumbersome. Second, in the practical applications we have in mind, the Fourier scale decomposition forms the theoretical backbone, hence the language in which results are to be presented and compared. The WR-basis, on the other hand, is most suited for efficient diagnostics of observational or simulation data on irregular meshes. What is most needed, therefore, is a procedure for converting WR-spectra to F-spectra.

In this paper, we have only considered random fields with constant spectral slopes. Similar techniques are expected to work if only a sufficiently large, asymptotically growing part of the spectrum satisfies a power law scaling. In the more general case of arbitrary spectra, analogs of (1) will become much more complicated and possibly analytically intractable. On the practical side, it may be possible to obtain the dependency between the spectral characteristics in the two bases empirically for some ensemble of random fields and then interpolate the results, using, e.g., machine learning or techniques from inverse problems as the translation from the Walsh–Rademacher to the Fourier spectrum will require deconvolution, i.e., is ill-posed, but may be regularized using assumptions on the smoothness of the spectrum as a function of k. We have already touched on non-constant slopes and complex spectra from a practical point of view in [14], but the corresponding theoretical analysis is the subject of ongoing research. In the future, we plan to expand the scaling analysis to other bases, e.g., to high-order polynomial bases. Moreover, we plan to expand the statistical analysis to more general distributions of ensembles of random fields.

Acknowledgements

We thank the anonymous reviewers for very useful comments and suggestions which helped improve the quality of the manuscript. This paper is a contribution to project M3 of the Collaborative Research Centre TRR 181 "Energy Transfer in Atmosphere and Ocean" funded by the Deutsche Forschungsgemeinschaft (DFG, German Research Foundation) under project number 274762653.

References

[1] A. S. Monin and A. M. Yaglom. *Statistical fluid mechanics: mechanics of turbulence. Vol. I.* Dover Publications, Inc., Mineola, NY, 2007. Translated from the 1965 Russian original, Edited and with a preface by John L. Lumley, English edition updated, augmented and revised by the authors, Reprinted from the 1971 edition.

[2] A. S. Monin and A. M. Yaglom. *Statistical fluid mechanics: mechanics of turbulence. Vol. II.* Dover Publications, Inc., Mineola, NY, 2007. Translated from the 1965 Russian original, Edited and with a preface by John L. Lumley, English edition updated, augmented and revised by the authors, Reprinted from the 1975 edition.

[3] N. J. Fine. On the Walsh functions. *Trans. Amer. Math. Soc.*, 65:372–414, 1949.

[4] M. Sadek and H. Aluie. Extracting the spectrum of a flow by spatial filtering. *Phys. Rev. Fluids*, 3:124610, 2018.

[5] A. N. Kolmogorov. The local structure of turbulence in incompressible viscous fluid for very large Reynolds numbers. *Proc. R. Soc. Lond. Ser. A Math. Phys. Eng. Sci.*, 434(1890):9–13, 1991. English translation of the original 1941 article.

[6] A. N. Kolmogorov. Dissipation of energy in the locally isotropic turbulence. *Proc. R. Soc. Lond. Ser. A Math. Phys. Eng. Sci.*, 434(1890):15–17, 1991. English translation of the original 1941 article.

[7] J. Callies and R. Ferrari. Interpreting energy and tracer spectra of upper-ocean turbulence in the submesoscale range (1–200 km). *J. Phys. Oceanogr.*, 43(11):2456–2474, 2013.

[8] J. M. Klymak and J. N. Moum. Oceanic isopycnal slope spectra. Part I: Internal waves. *J. Phys. Oceanogr.*, 37(5):1215–1231, 2007.

[9] C. Garrett and W. Munk. Space-time scales of internal waves. *Geophys. Fluid Dyn.*, 3(3):225–264, 1972.

[10] C. Garrett and W. Munk. Space-time scales of internal waves: A progress report. *J. Geophys. Res.*, 80(3):291–297, 1975.

[11] R. H. Kraichnan. Inertial ranges in two-dimensional turbulence. *Phys. Fluids*, 10:1417–1423, 1967.

[12] C. E. Leith. Diffusion approximation for two-dimensional turbulence. *Phys. Fluids*, 11:671–673, 1968.

[13] G. K. Batchelor. Computation of energy spectrum in homogeneous two-dimensional turbulence. *Phys. Fluids Suppl.*, 12, II:233–239, 1969.

[14] S. Juricke, K. Bellinghausen, S. D. Danilov, A. A. Kutsenko, and M. Oliver. Scale analysis on unstructured grids: Kinetic energy and dissipation power spectra on triangular meshes. *J. Adv. Model. Earth Syst.*, 15:e2022MS003280, 2023.

[15] X. San Liang. Canonical transfer and multiscale energetics for primitive and quasigeostrophic atmospheres. *J. Atmos. Sci.*, 73:4439–4468, 2016.

[16] P. Baldi, G. Kerkyacharian, D. Marinucci, and D. Picard. Asymptotics for spherical needlets. *Ann. Statist.*, 37(3):1150–1171, 2009.

[17] V. Cammarota and D. Marinucci. On the limiting behaviour of needlets polyspectra. *Ann. Inst. Henri Poincaré Probab. Stat.*, 51(3):1159–1189, 2015.

[18] C. Durastanti, D. Marinucci, and G. Peccati. Normal approximations for wavelet coefficients on spherical Poisson fields. *J. Math. Anal. Appl.*, 409(1):212–227, 2014.

[19] R. Shevchenko and A. P. Todino. Asymptotic behaviour of level sets of needlet random fields. *Stochastic Process. Appl.*, 155:268–318, 2023.

[20] R. Shevchenko. Quadratic variations for Gaussian isotropic random fields on the sphere. *arXiv:2105.11970*, 2021.

[21] V. V. Jikov, S. M. Kozlov, and O. A. Oleĭnik. *Homogenization of differential operators and integral functionals.* Springer-Verlag, Berlin, 1994. Translated from the Russian by G. A. Yosifian.

[22] W. Feller. *An introduction to probability theory and its applications. Vol. I.* John Wiley & Sons, Inc., New York-London-Sydney, third edition, 1968.

[23] M. Reed and B. Simon. *Methods of modern mathematical physics. IV. Analysis of operators.* Academic Press [Harcourt Brace Jovanovich, Publishers], New York-London, 1978.

[24] H. Rademacher. Einige Sätze über Reihen von allgemeinen Orthogonalfunktionen. *Math. Ann.*, 87(1-2):112–138, 1922.
[25] J. L. Walsh. A closed set of normal orthogonal functions. *Amer. J. Math.*, 45(1):5–24, 1923.
[26] A. M. Yaglom. *Correlation Theory of Stationary and Related Random Functions. Basic Results*, volume 1. Springer, 1987.